Paleoceanography and Paleoclimatology

Supporting Information for

Incoherency in Central American hydroclimate proxy records spanning the last millennium

Jonathan Obrist-Farner[1], Byron Steinman[2], Nathan Stansell[3], and Jeremy Maurer[1]

1. Geosciences and Geological and Petroleum Engineering Department, Missouri University of Science and Technology, USA.
2. Large Lakes Observatory and Department of Earth and Environmental Sciences, University of Minnesota Duluth, USA.
3. Department of Geology and Environmental Geosciences, Northern Illinois University, USA.

Contents of this file

Figures S1 to S27

Additional Supporting Information (Files uploaded separately)

Tables S1. Radiocarbon dates for the core from Lake Petén Itzá.
Table S2. Radiocarbon dates for the core from Lake Izabal.
Table S3. Elemental abundances for the Petén Itzá core in counts per second.
Table S4. Elemental abundances for the Izabal core in counts per second.

Introduction

This document contains supplementary figures and references as supporting information. Additional data tables are provided as separate excel files. The methodology used to generate the following figures is described in the main text of the manuscript.

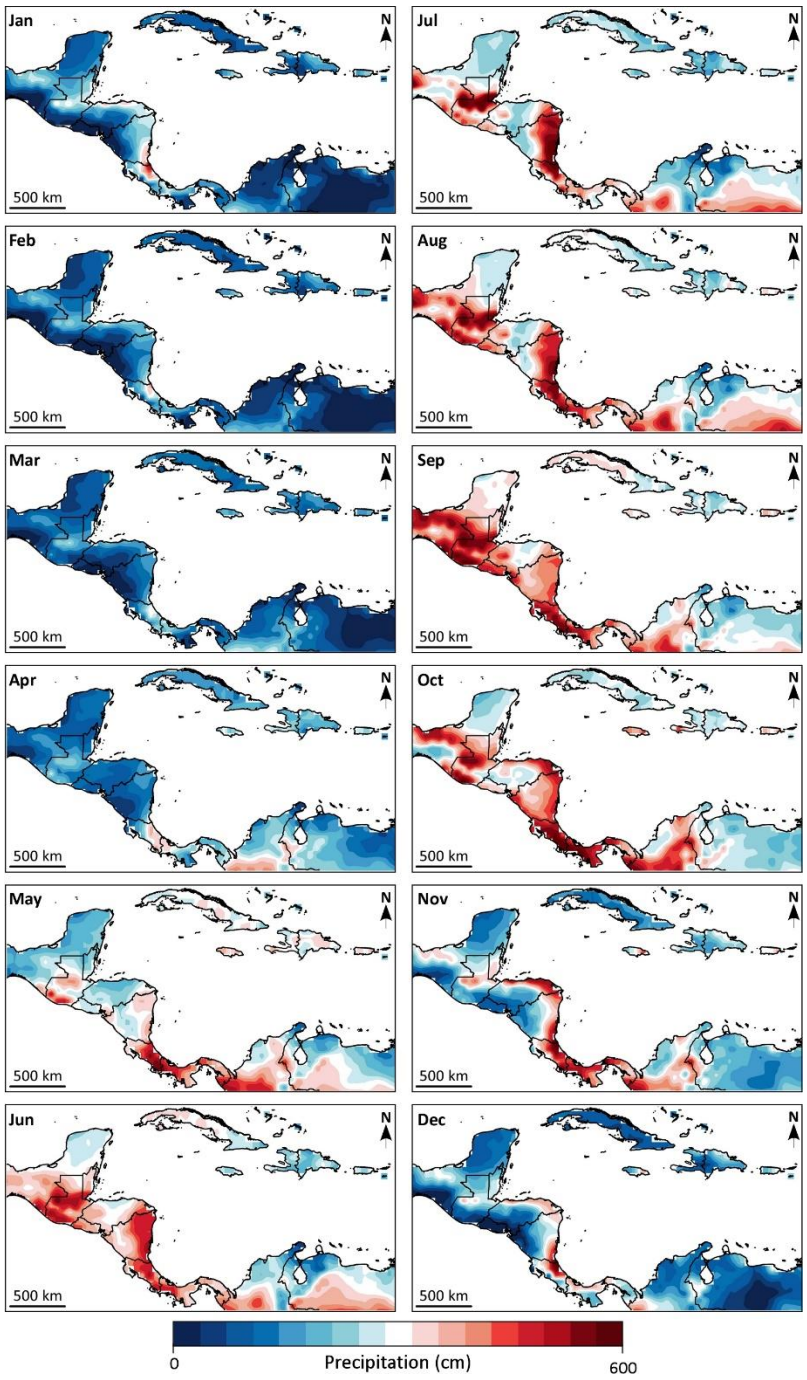

Figure S1. Maps of Central America, the Caribbean, and northern South America showing mean monthly precipitation based on three gridded data products (Willmott & Matsuura, 2001; Schneider et al., 2011; Harris et al., 2014) spanning the period 1966-2016 CE.

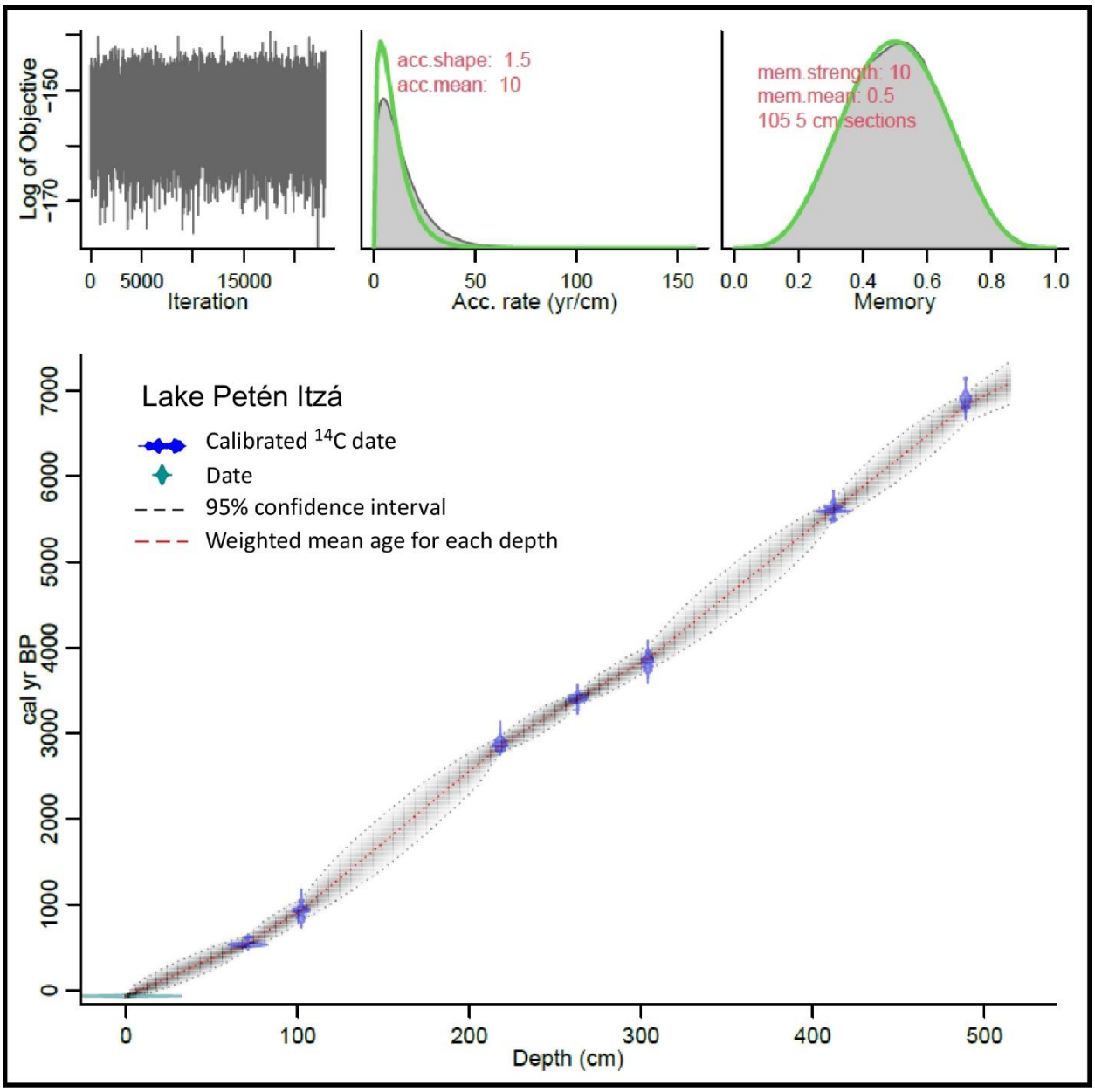

Figure S2. Age-depth model for Lake Petén Itzá (this study; Obrist-Farner & Rice, 2019). All radiocarbon dates were obtained from charcoal/wood fragments. Red line shows the best-fit model based on weighted mean ages, and stippled gray lines show 95% confidence intervals. All dates were calibrated using IntCal20 (Reimer et al., 2020). The age-depth model was generated using Bacon (Blaauw & Christen, 2011). Raw data provided in supplementary table 1.

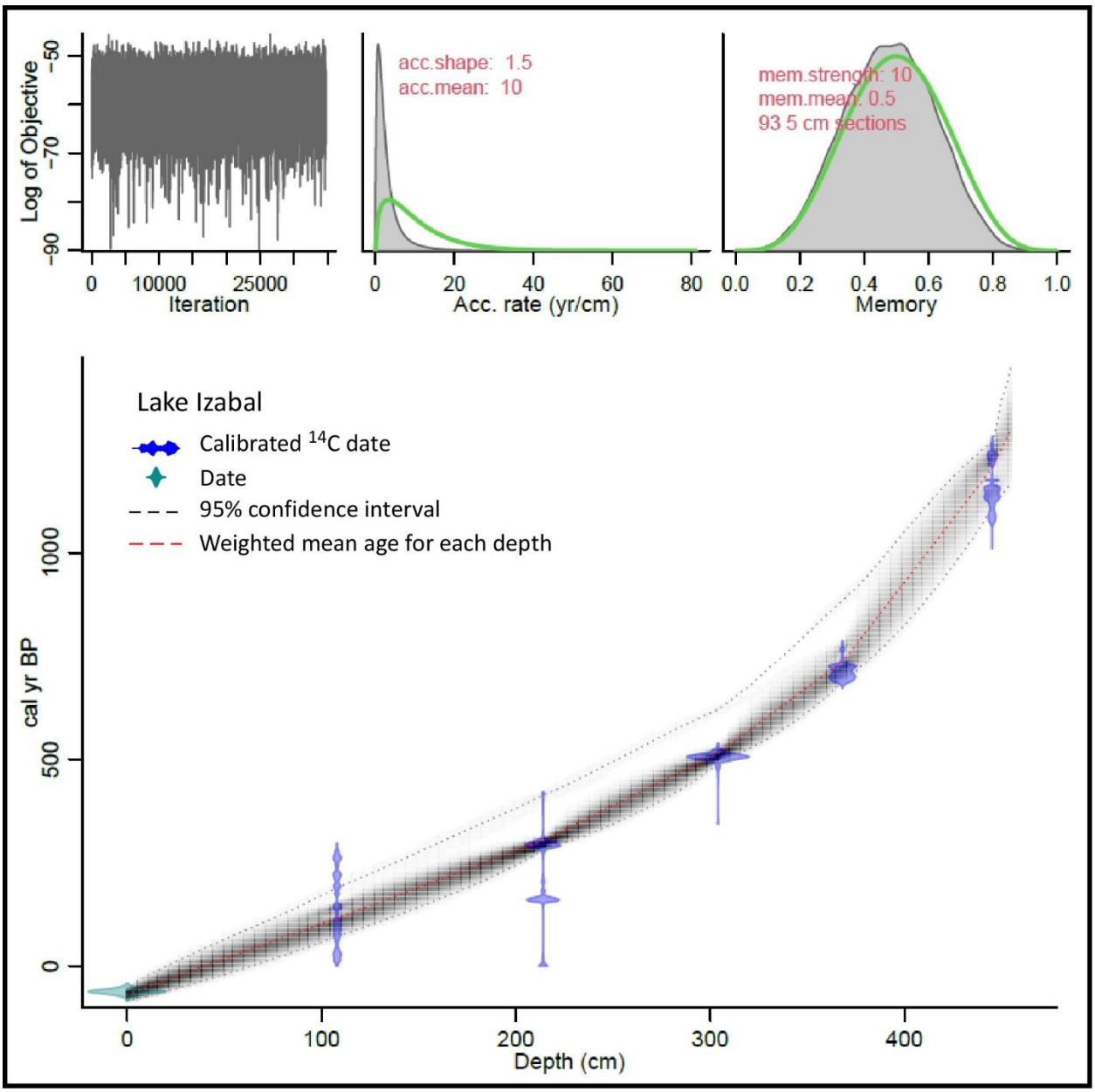

Figure S3. Age-depth model for Lake Izabal (this study; Hernández et al., 2020). All radiocarbon dates were obtained from charcoal/wood fragments. Red line shows the best-fit model based on weighted mean ages, and stippled gray lines show 95% confidence intervals. All dates were calibrated using IntCal20 (Reimer et al., 2020). The age-depth model was generated using Bacon (Blaauw & Christen, 2011). Raw data provided in supplementary table 2.

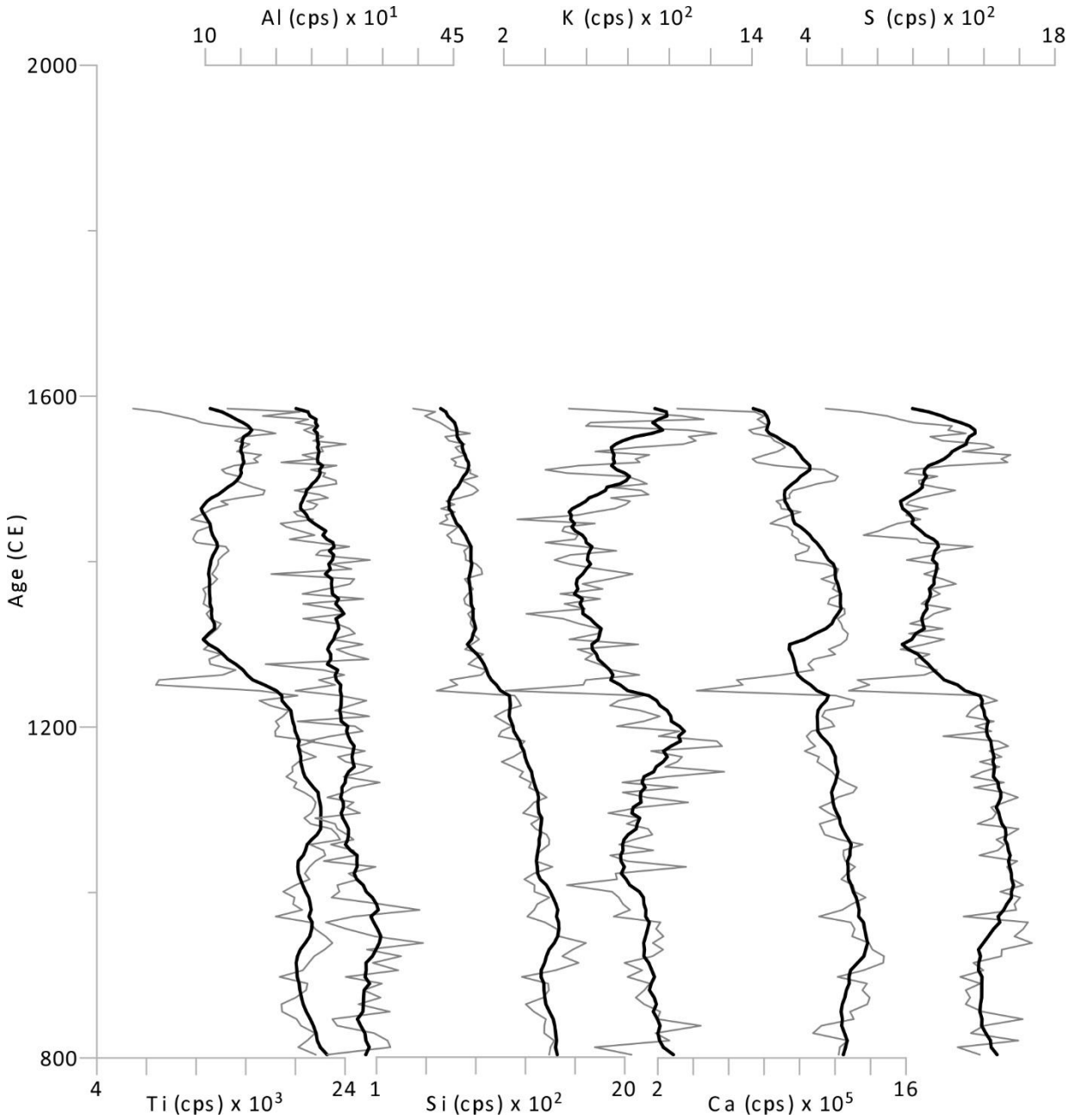

Figure S4. Proxy data versus age for the Lake Petén Itzá core. Figure shows elemental abundances in counts per second (cps). The gray line shows the unfiltered data and the black lines show the 10 point moving average. Raw data provided in supplementary table 3.

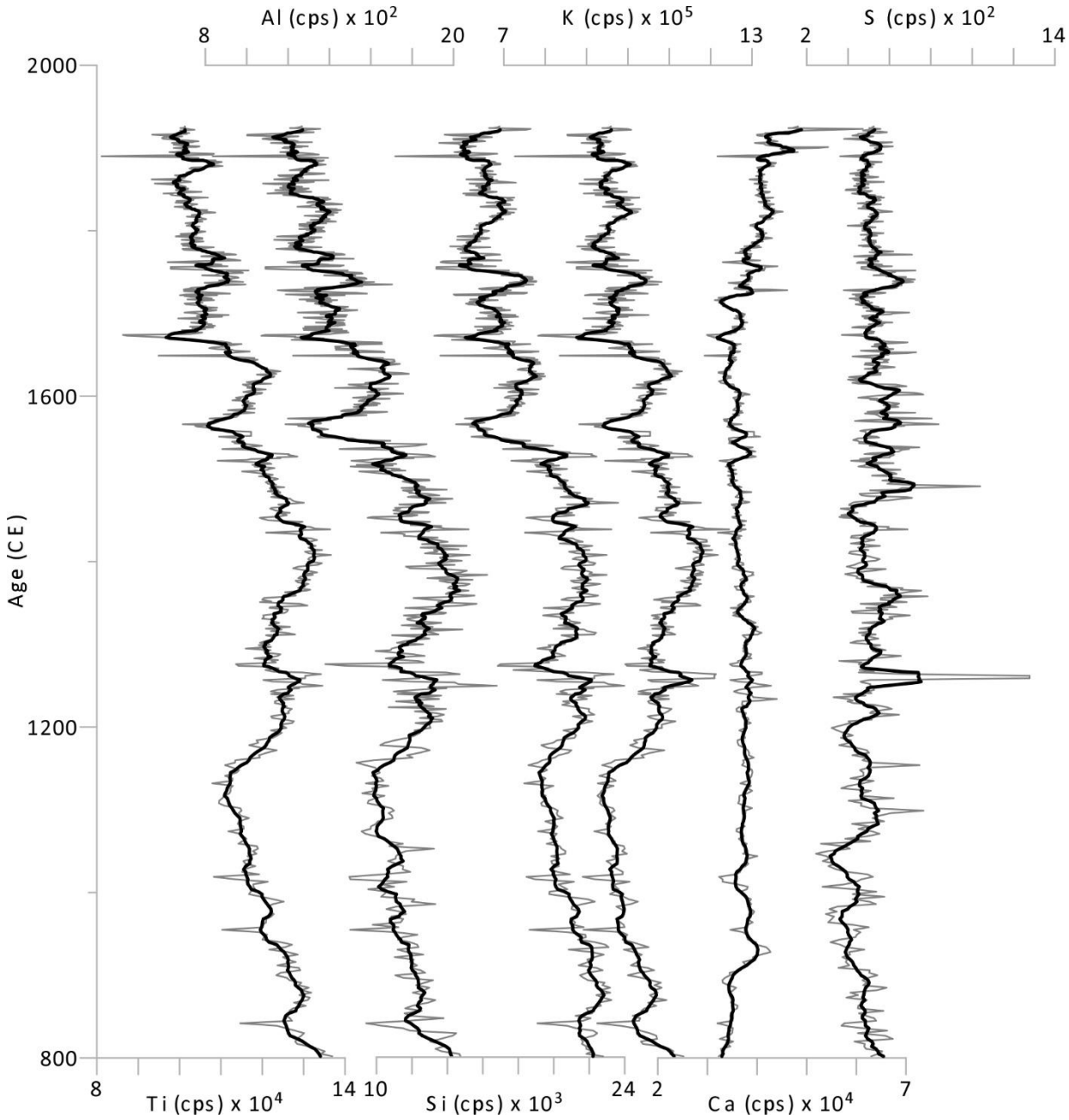

Figure S5. Proxy data versus age for the Lake Izabal core. Figure shows elemental abundances in counts per second (cps). The gray line shows the unfiltered data and the black lines show the 10 point moving average. Raw data provided in supplementary table 4.

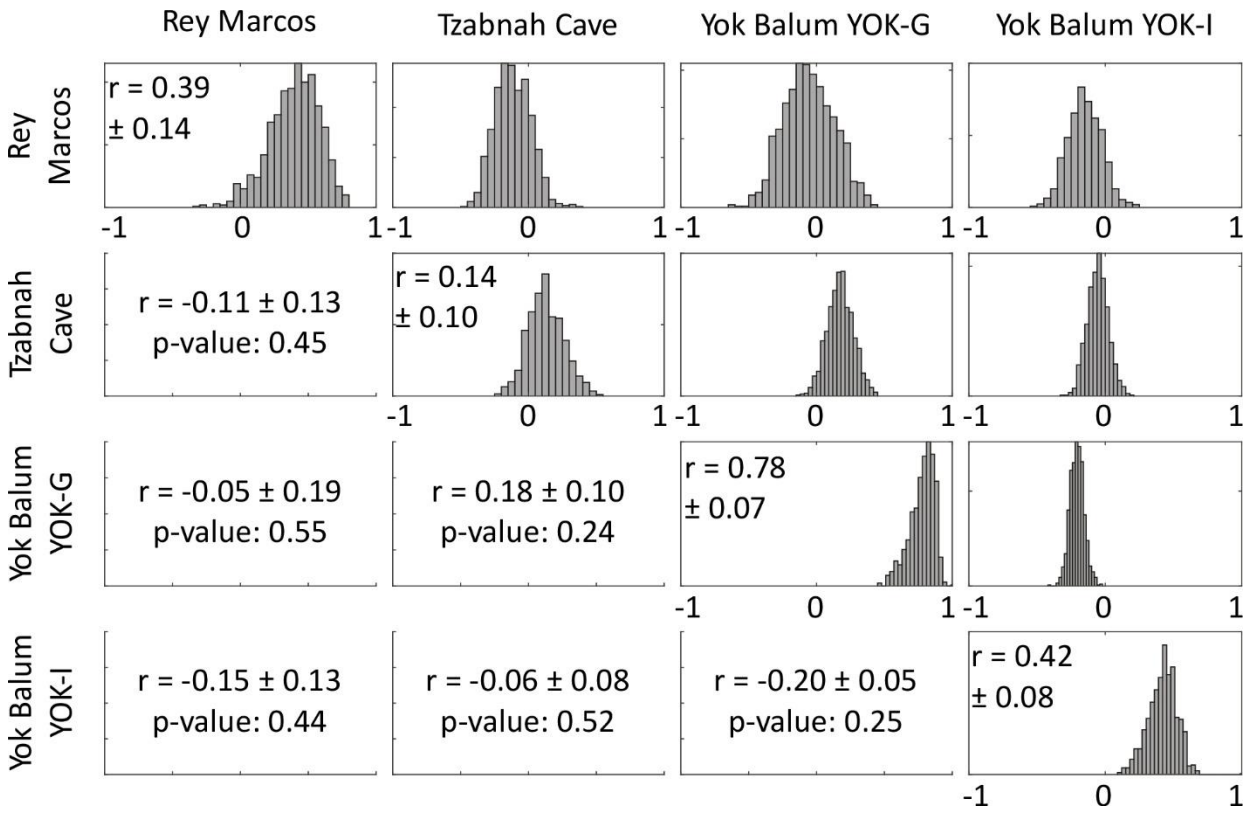

Figure S6. Matrix showing the range of correlation values (upper right) for all speleothem record realizations used in this study utilizing 1000 age-proxy pairs. The diagonal quantifies the uncertainties in the age-depth model; for example, an age-depth model with no uncertainty would have correlation equal to 1. The distribution represents how correlated the 1000 age-proxy realizations are to each other (see Supplementary Material). The lower left shows mean correlation values, ±1σ, and mean p-values for the records analyzed. The $\delta^{18}O$ records been multiplied by negative one so that positive correlation indicates consistent behavior between proxy sites.

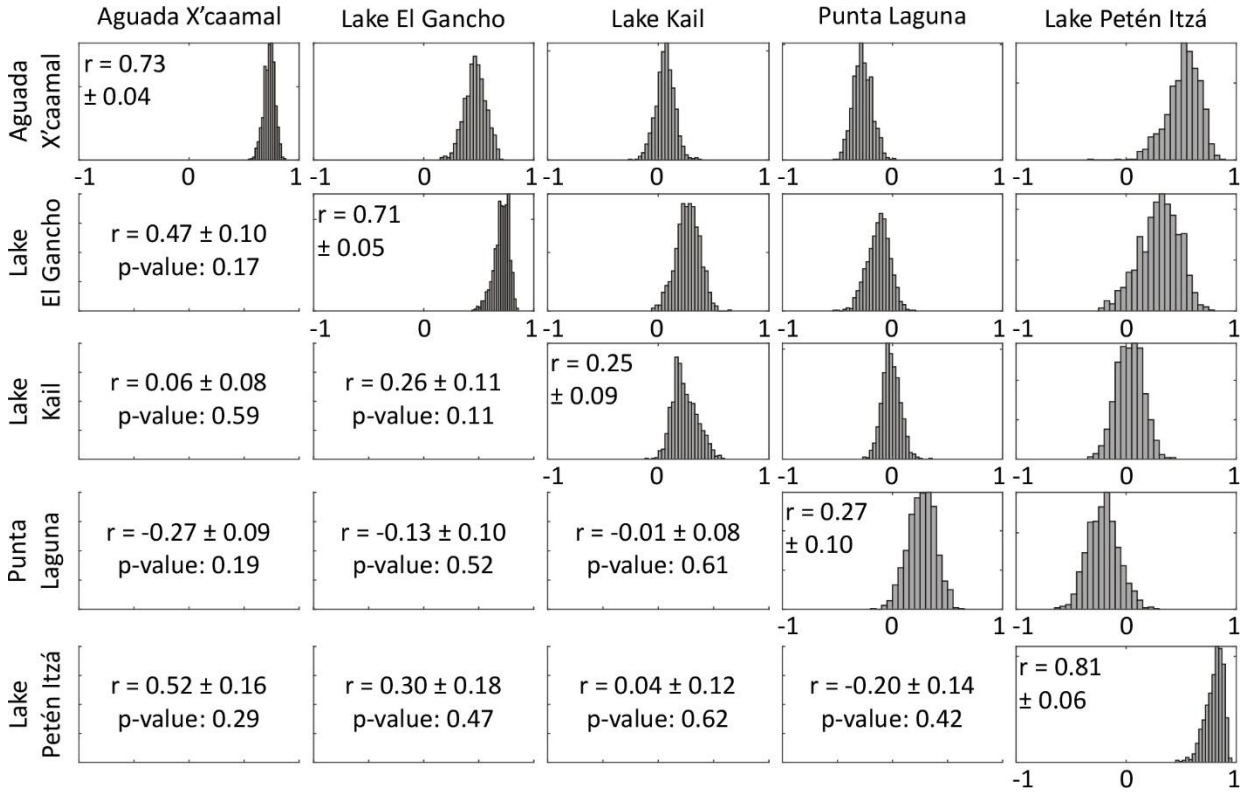

Figure S7. Matrix showing the range of correlation values (upper right) for all small and closed lacustrine basin record realizations used in this study utilizing 1000 age-proxy pairs. The diagonal quantifies the uncertainties in the age-depth model; for example, an age-depth model with no uncertainty would have correlation equal to 1. The distribution represents how correlated the 1000 age-proxy realizations are to each other (see Supplementary Material). The lower left shows mean correlation values, ±1σ, and mean p-values for the records analyzed. The $\delta^{18}O$ records been multiplied by negative one so that positive correlation indicates consistent behavior between proxy sites.

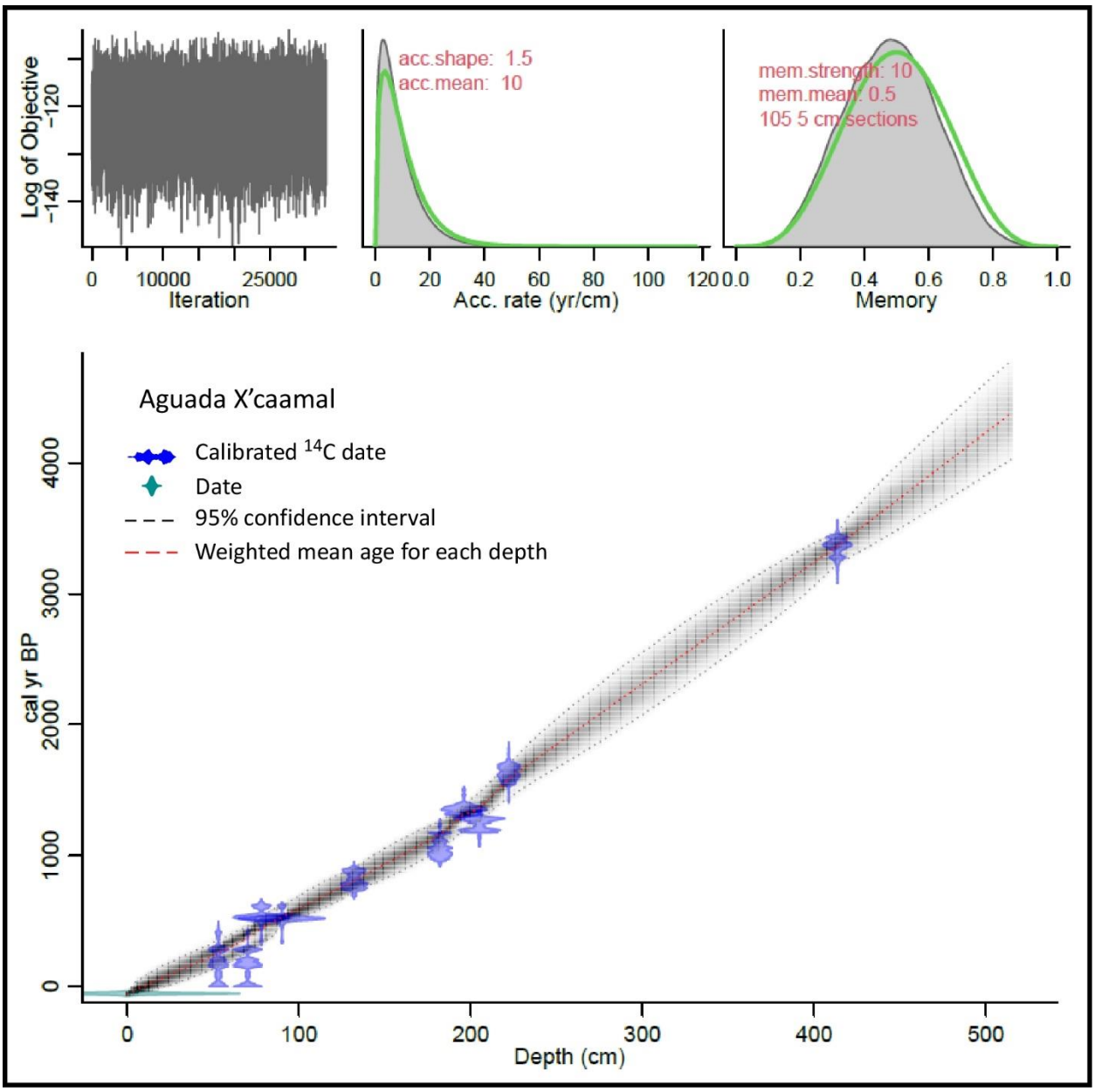

Figure S8. Age-depth model for Aguada X'caamal (Hodell et al., 2005). All radiocarbon dates are from terrestrial organic material. Red line shows the best-fit model based on weighted mean ages, and stippled gray lines show 95% confidence intervals. All dates were calibrated using IntCal20 (Reimer et al., 2020). The age-depth model was generated using Bacon (Blaauw & Christen, 2011).

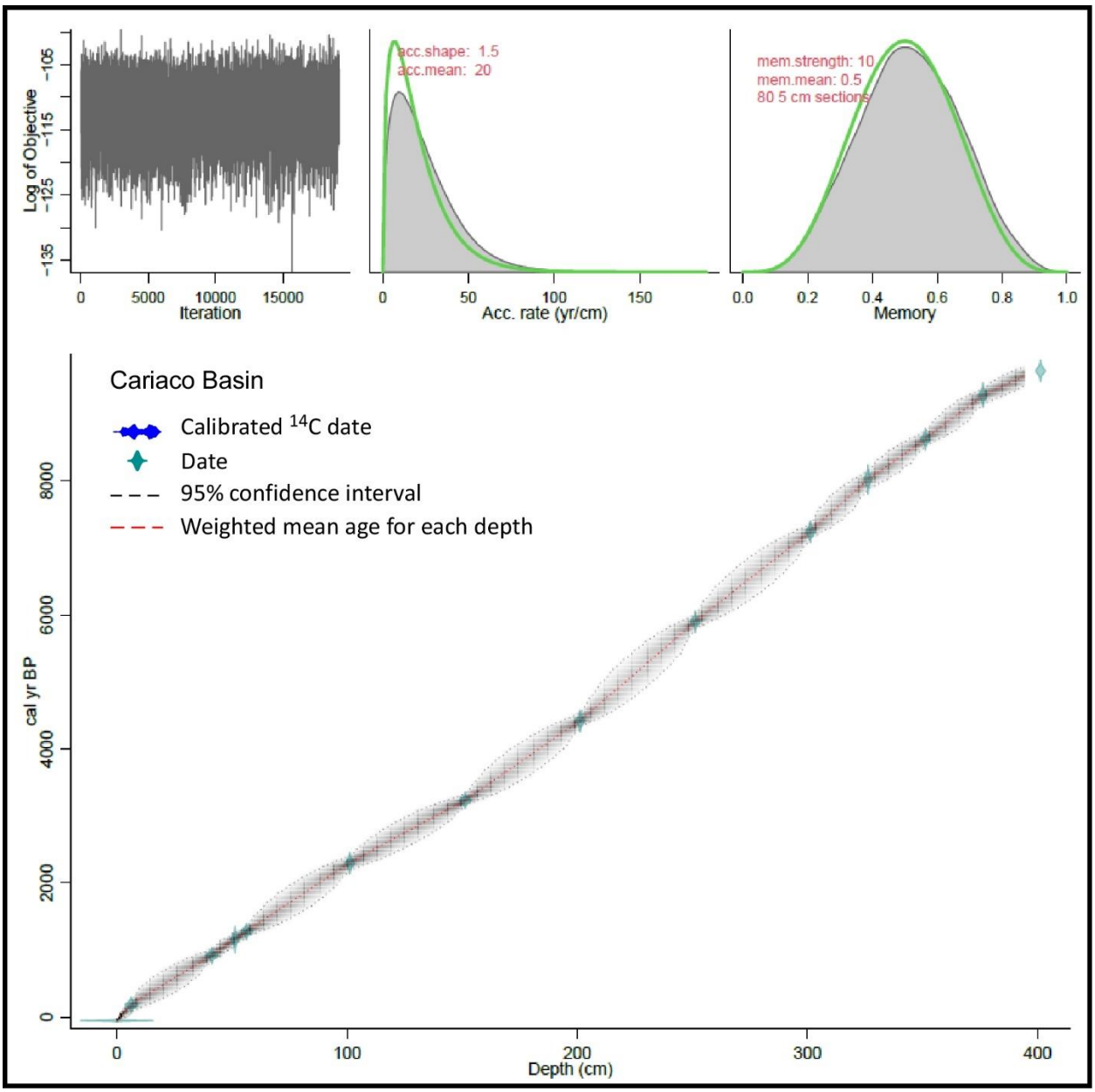

Figure S9. Age-depth model for the Cariaco Basin sediment core (Haug et al., 2001). All radiocarbon dates are from planktic foraminifera and corrected from the marine reservoir effect. Red line shows the best-fit model based on weighted mean ages, and stippled gray lines show 95% confidence intervals. The age-depth model was generated using Bacon (Blaauw & Christen, 2011).

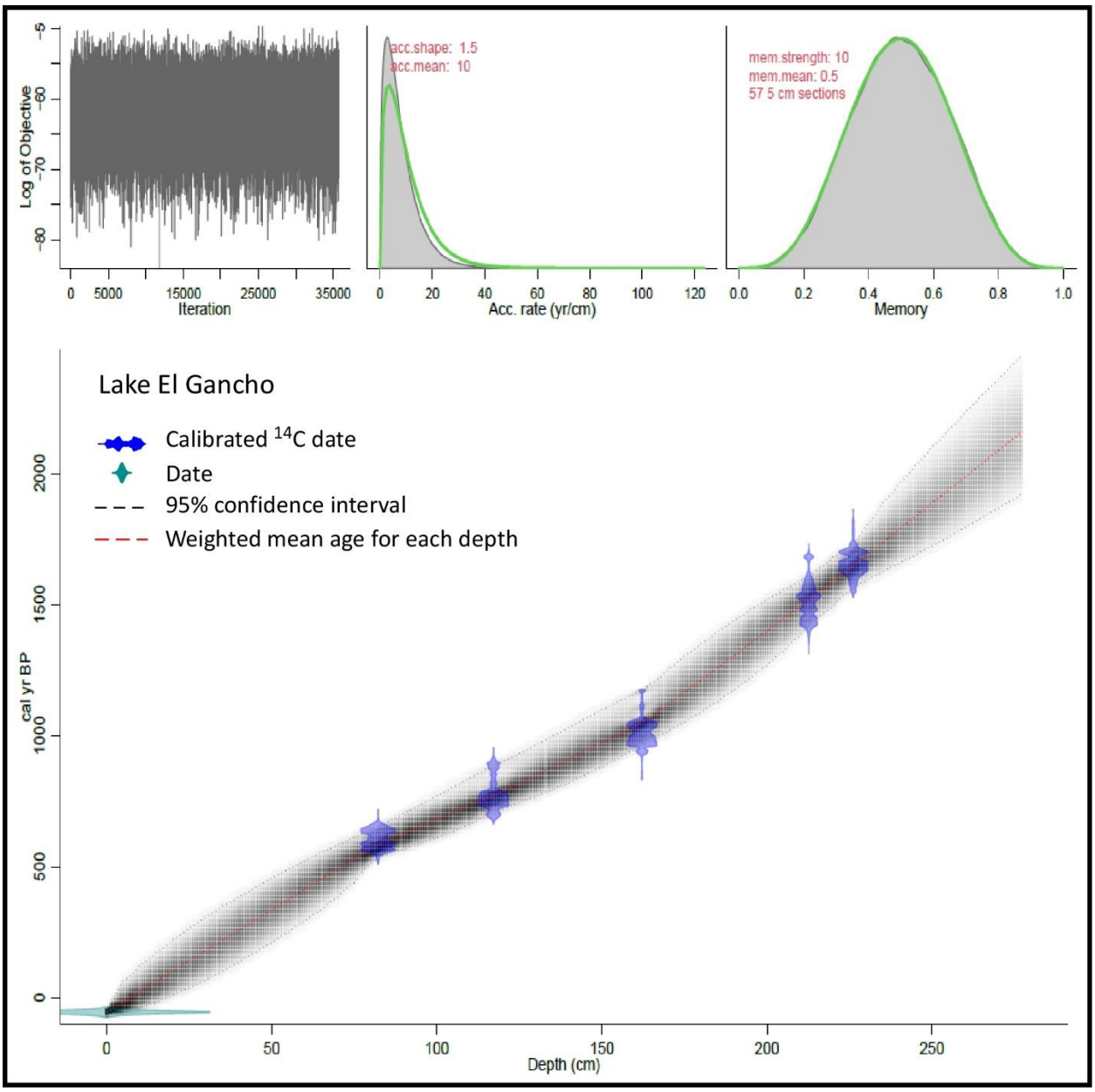

Figure S10. Age-depth model for Lake El Gancho (Stansell et al., 2013). All radiocarbon dates were obtained from charcoal fragments. Red line shows the best-fit model based on weighted mean ages, and stippled gray lines show 95% confidence intervals. All dates were calibrated using IntCal20 (Reimer et al., 2020). The age-depth model was generated using Bacon (Blaauw & Christen, 2011).

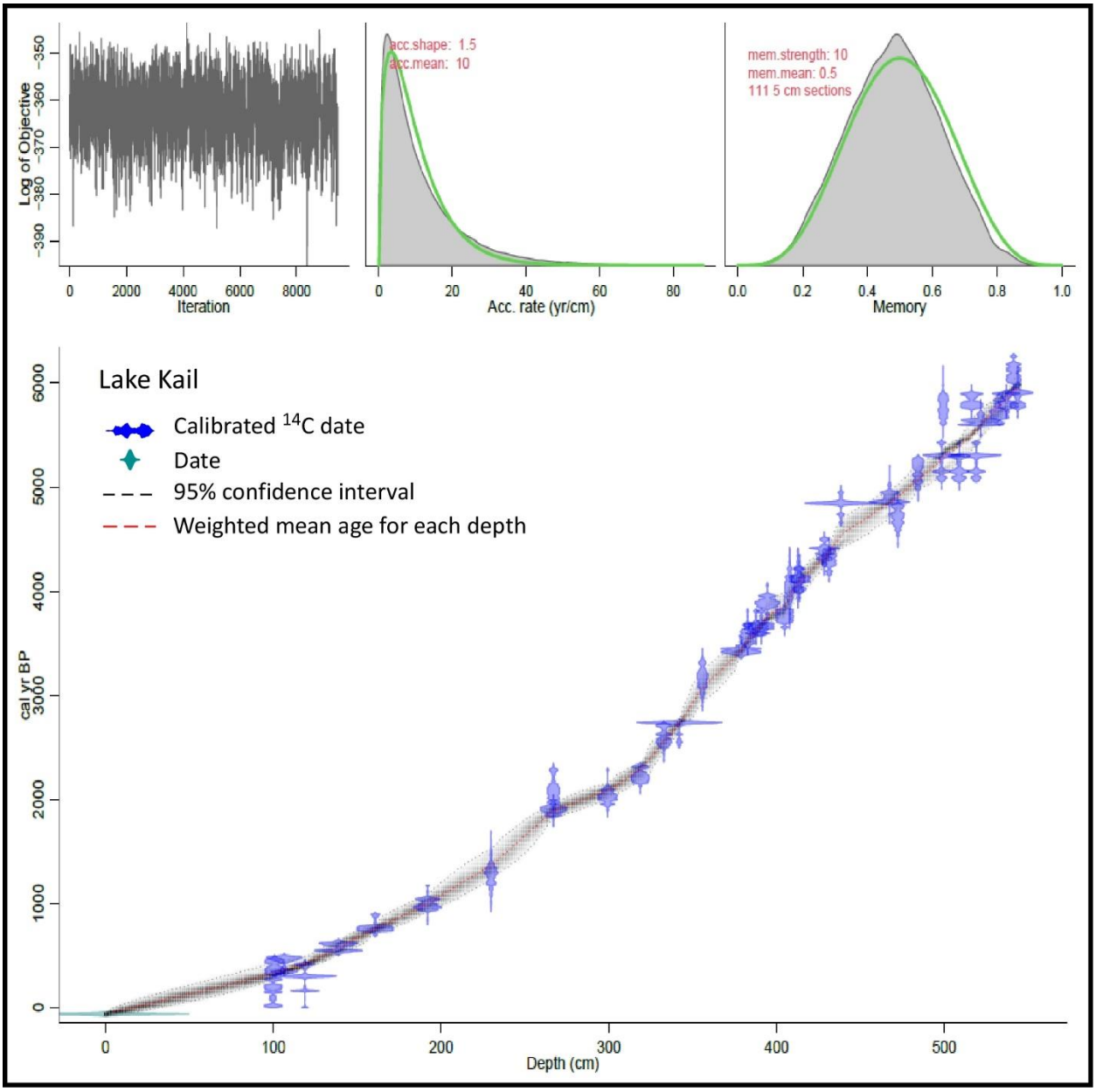

Figure S11. Age-depth model for Lake Kail (Stansell et al., 2020). All radiocarbon dates were obtained from charcoal and leaf fragments. Red line shows the best-fit model based on weighted mean ages, and stippled gray lines show 95% confidence intervals. All dates were calibrated using IntCal20 (Reimer et al., 2020). The age-depth model was generated using Bacon (Blaauw & Christen, 2011).

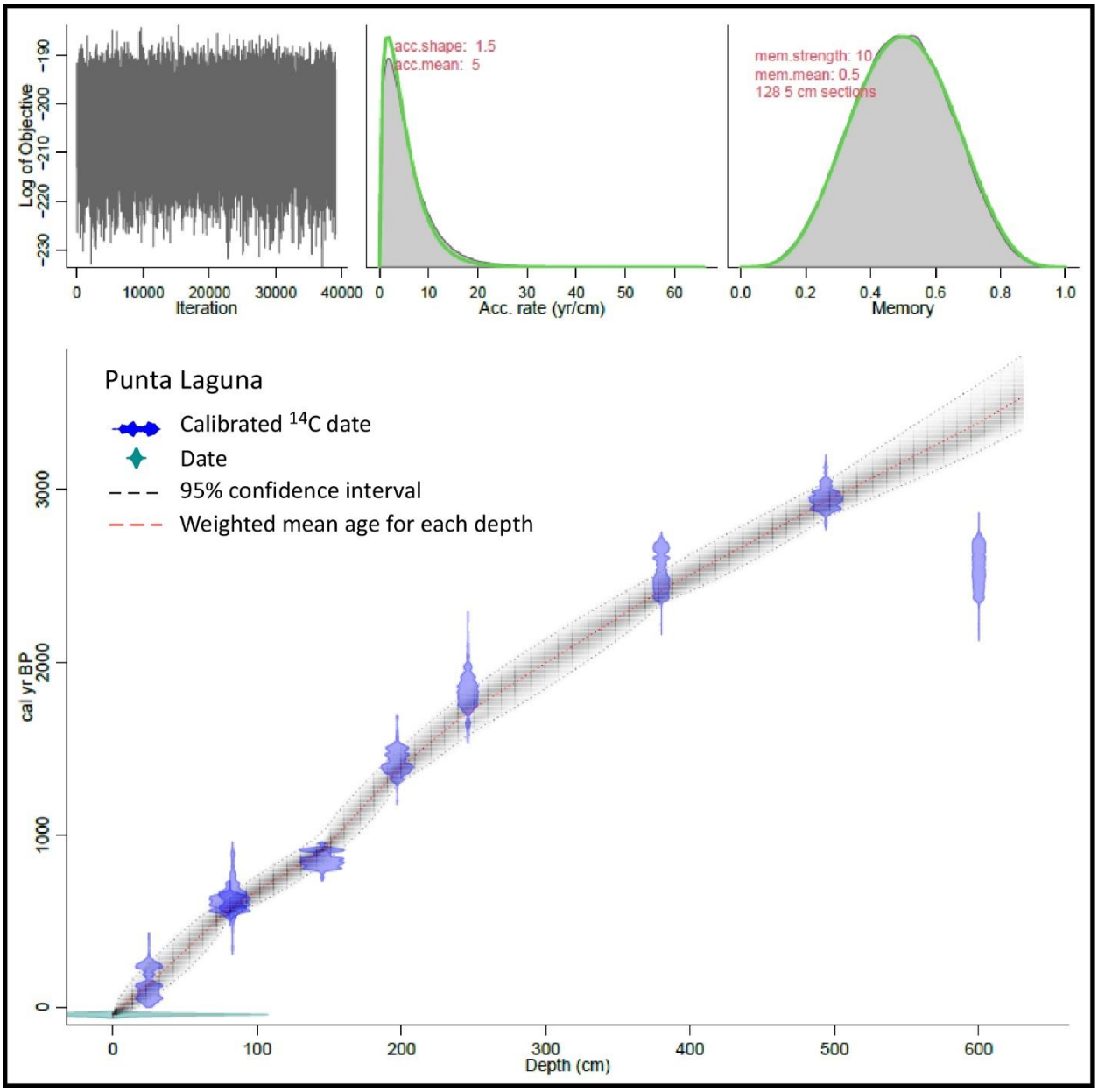

Figure S12. Age-depth model for Punta Laguna (Curtis et al., 1996). Radiocarbon dates were obtained from five terrestrial wood samples and four from shell material. Shell radiocarbon dates were corrected for hard water lake error for Punta Laguna. Red line shows the best-fit model based on weighted mean ages, and stippled gray lines show 95% confidence intervals. All dates were calibrated using IntCal20 (Reimer et al., 2020). The age-depth model was generated using Bacon (Blaauw & Christen, 2011).

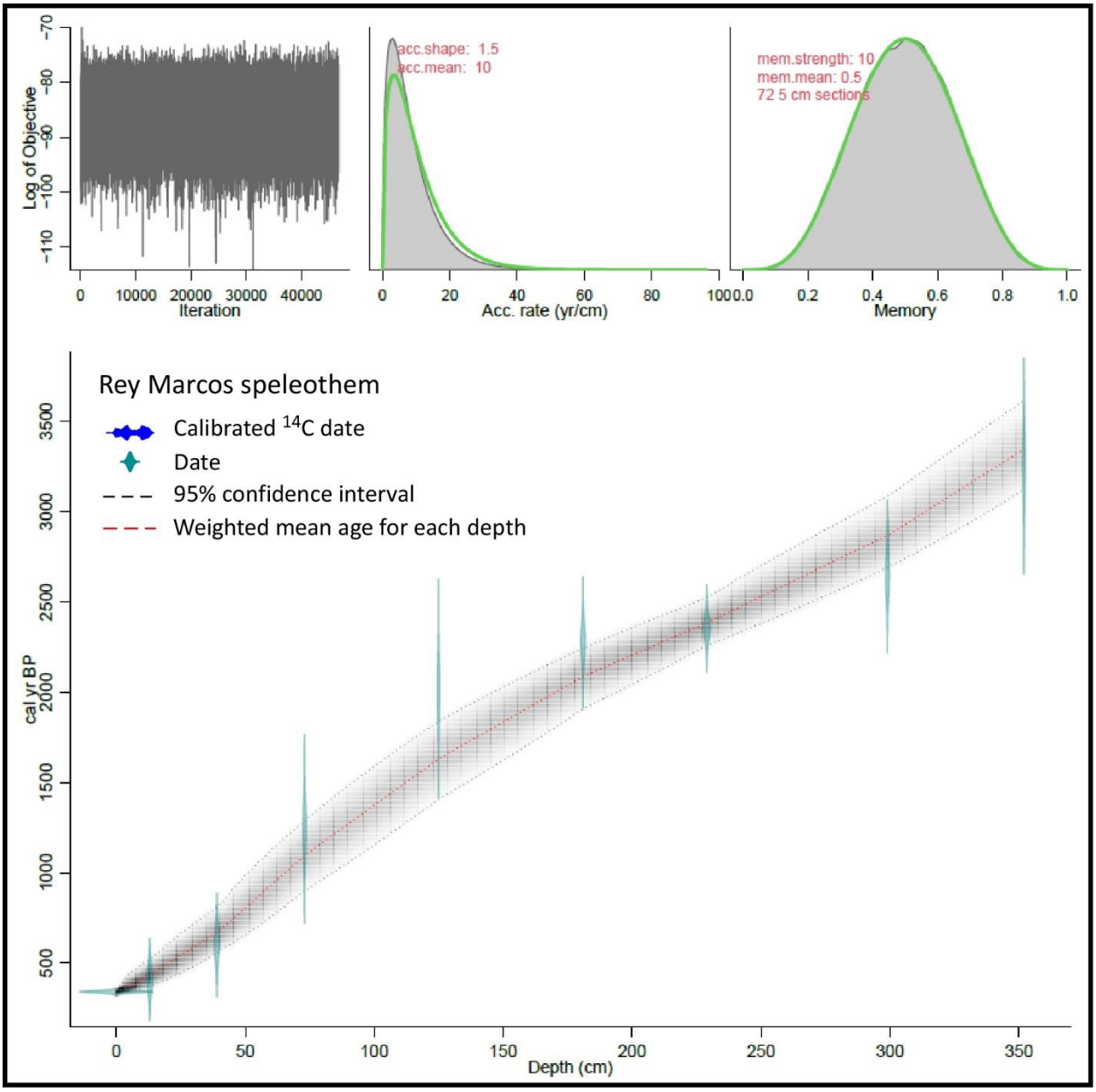

Figure S13. Age-depth model for the Rey Marcos speleothem (Winter et al., 2020). The age model is based on 21 U/Th dates. radiocarbon dates were obtained from charcoal/wood fragments. Red line shows the best-fit model based on weighted mean ages, and stippled gray lines show 95% confidence intervals. The age-depth model was generated using Bacon (Blaauw & Christen, 2011). Model generated is only for the first 4000 years of the record.

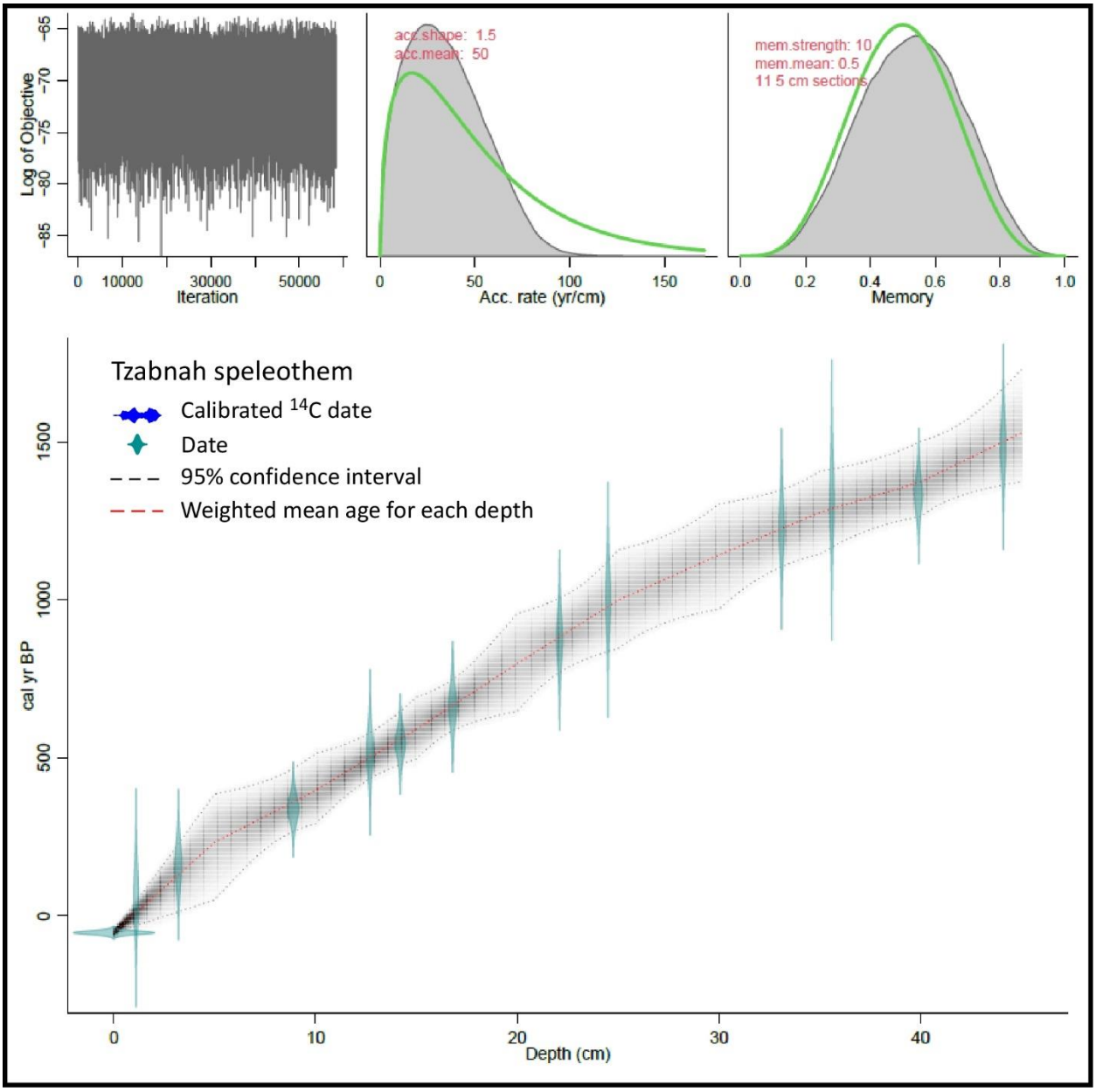

Figure S14. Age-depth model for the Tzabnah speleothem (Medina-Elizalde et al., 2010). The age model is based on 12 U/Th dates. Red line shows the best-fit model based on weighted mean ages, and stippled gray lines show 95% confidence intervals. The age-depth model was generated using Bacon (Blaauw & Christen, 2011).

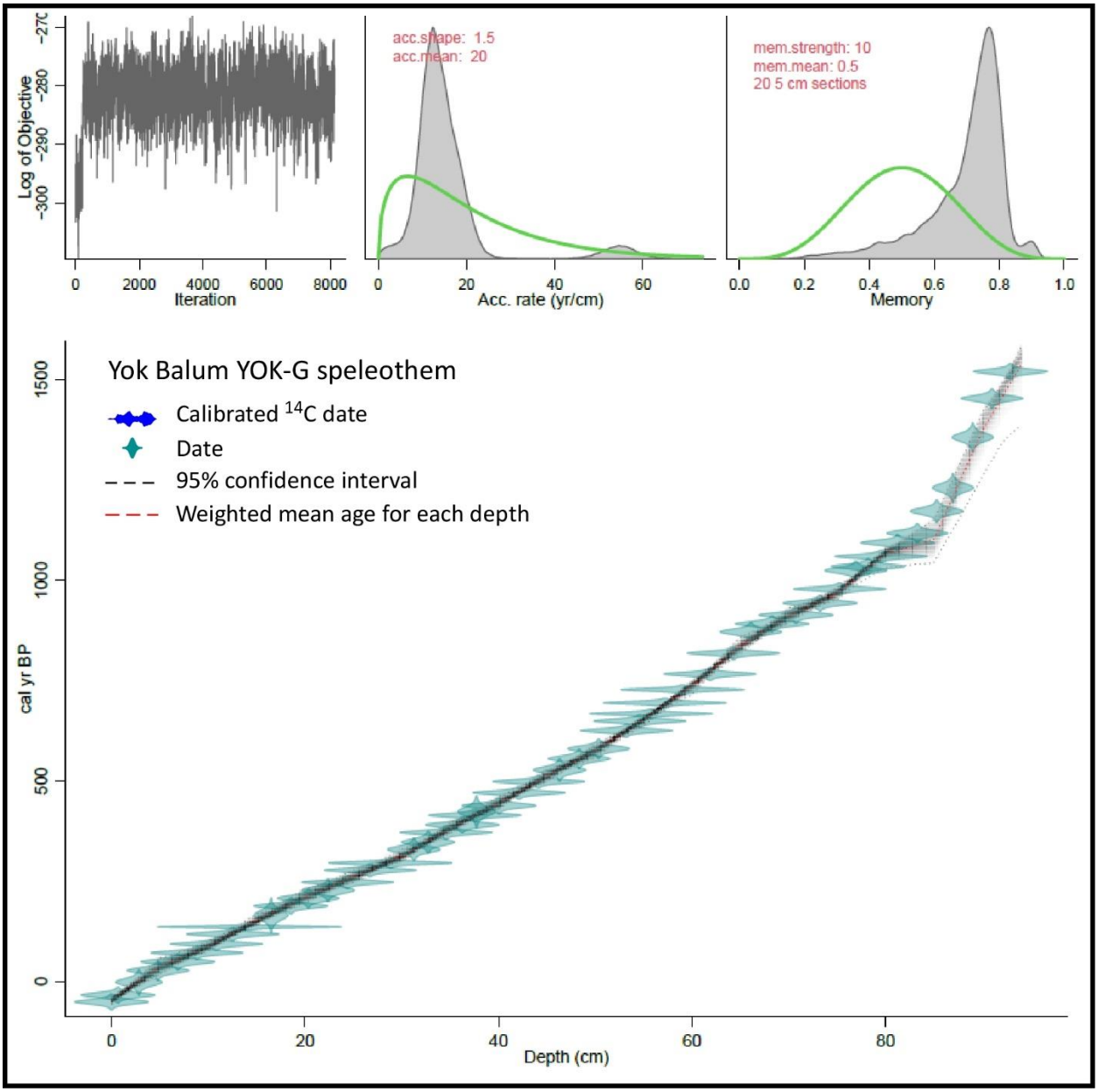

Figure S15. Age-depth model for the YOK-G speleothem (Asmerom et al., 2020). The age model is based on 52 U/Th dates. Red line shows the best-fit model based on weighted mean ages, and stippled gray lines show 95% confidence intervals. The age-depth model was generated using Bacon (Blaauw & Christen, 2011).

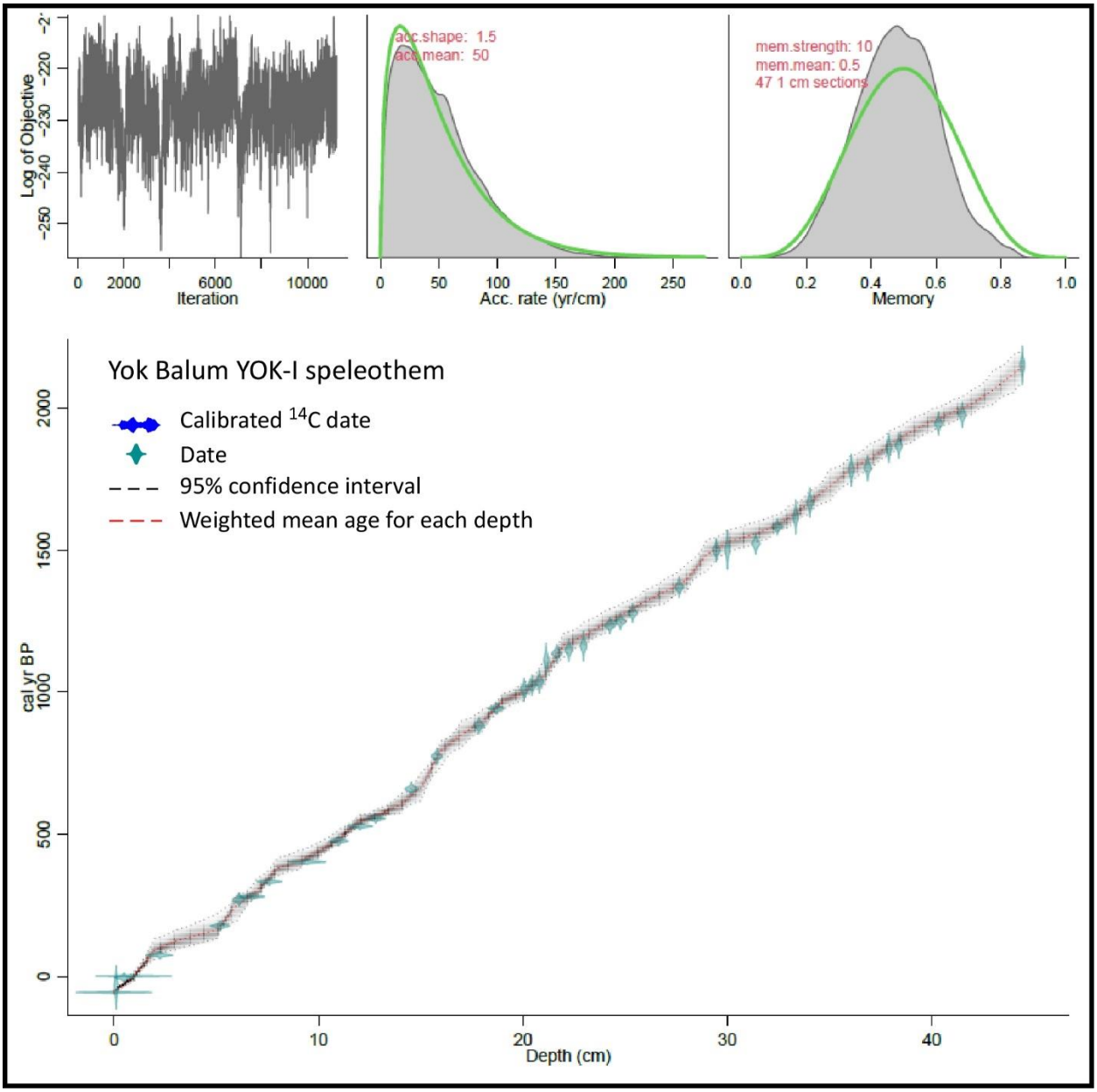

Figure S16. Age-depth model for YOK-I (Kennett et al., 2012). The age model is based on 40 U/Th dates. Red line shows the best-fit model based on weighted mean ages, and stippled gray lines show 95% confidence intervals. The age-depth model was generated using Bacon (Blaauw & Christen, 2011).

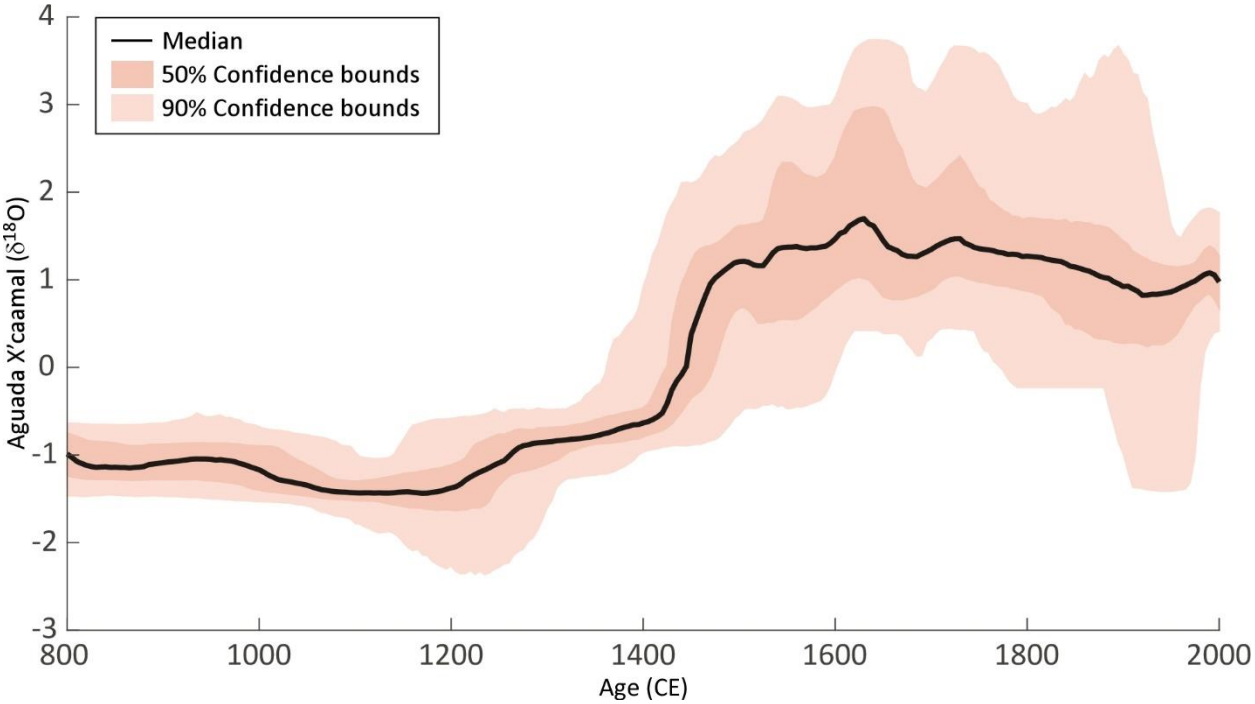

Figure S17. Median, 50% and 90% confidence bounds for the Aguada X'caamal $\delta^{18}O$ record (Hodell et al., 2005). The plot shows the range of proxy values for 1000 age-depth models (same set of models used for the correlation analysis shown in Figure 5). Note that the graph shows the unconditional probability at each time step. That is, the graph does not represent correlations between time steps.

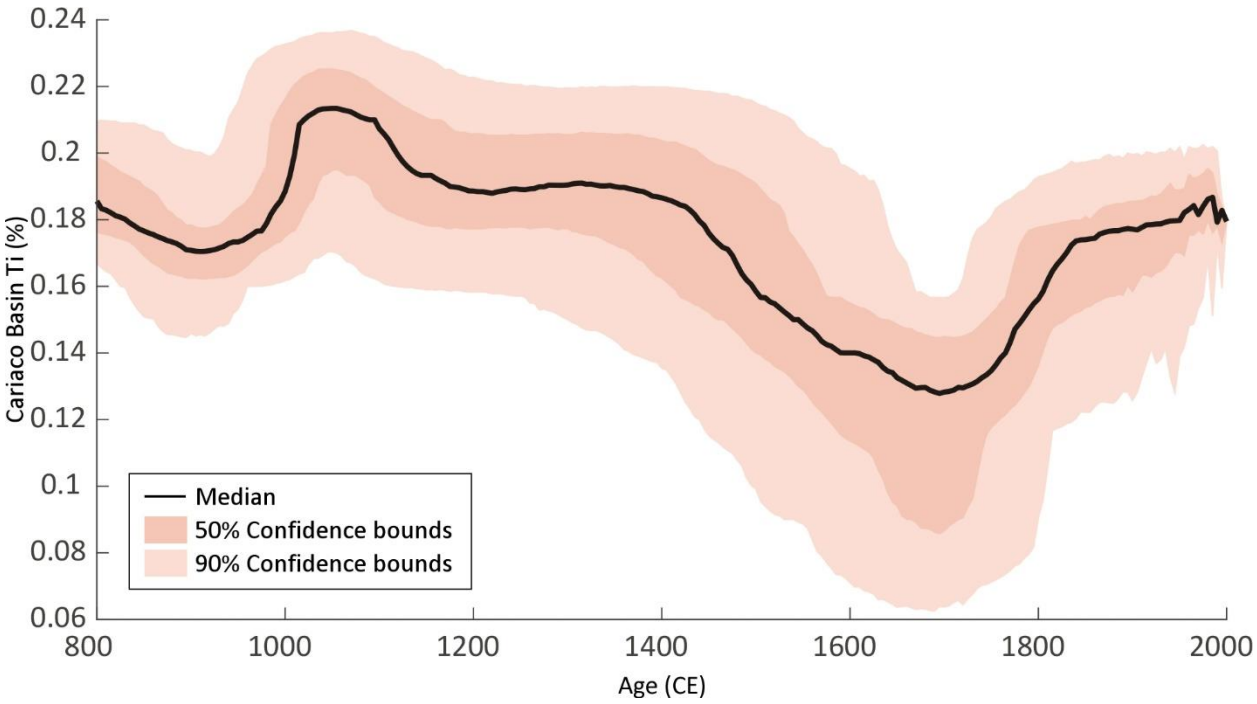

Figure S18. Median, 50% and 90% confidence bounds for the Cariaco Basin titanium record (Haug et al., 2001). The plot shows the range of proxy values for 1000 age-depth models (same set of models used for the correlation analysis shown in Figure 5). Note that the graph shows the unconditional probability at each time step. That is, the graph does not represent correlations between time steps.

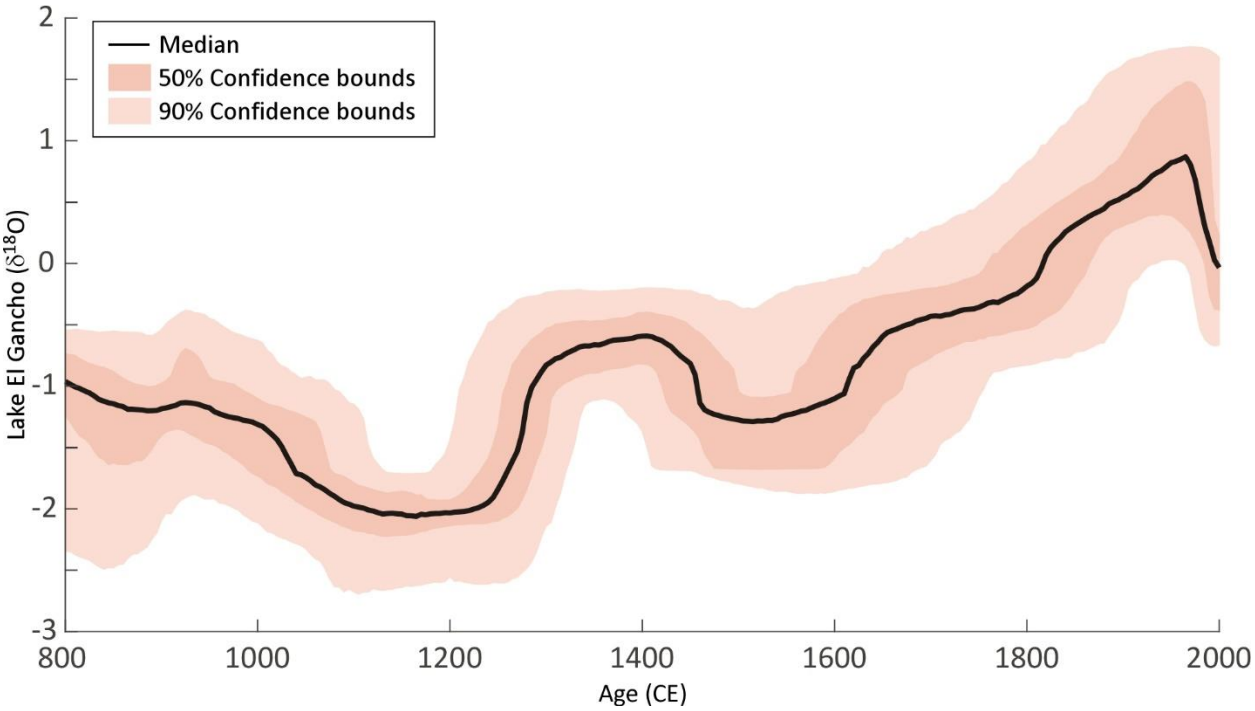

Figure S19. Median, 50% and 90% confidence bounds for the Lake El Gancho $\delta^{18}O$ record (Stansell et al., 2013). The plot shows the range of proxy values for 1000 age-depth models (same set of models used for the correlation analysis shown in Figure 5). Note that the graph shows the unconditional probability at each time step. That is, the graph does not represent correlations between time steps.

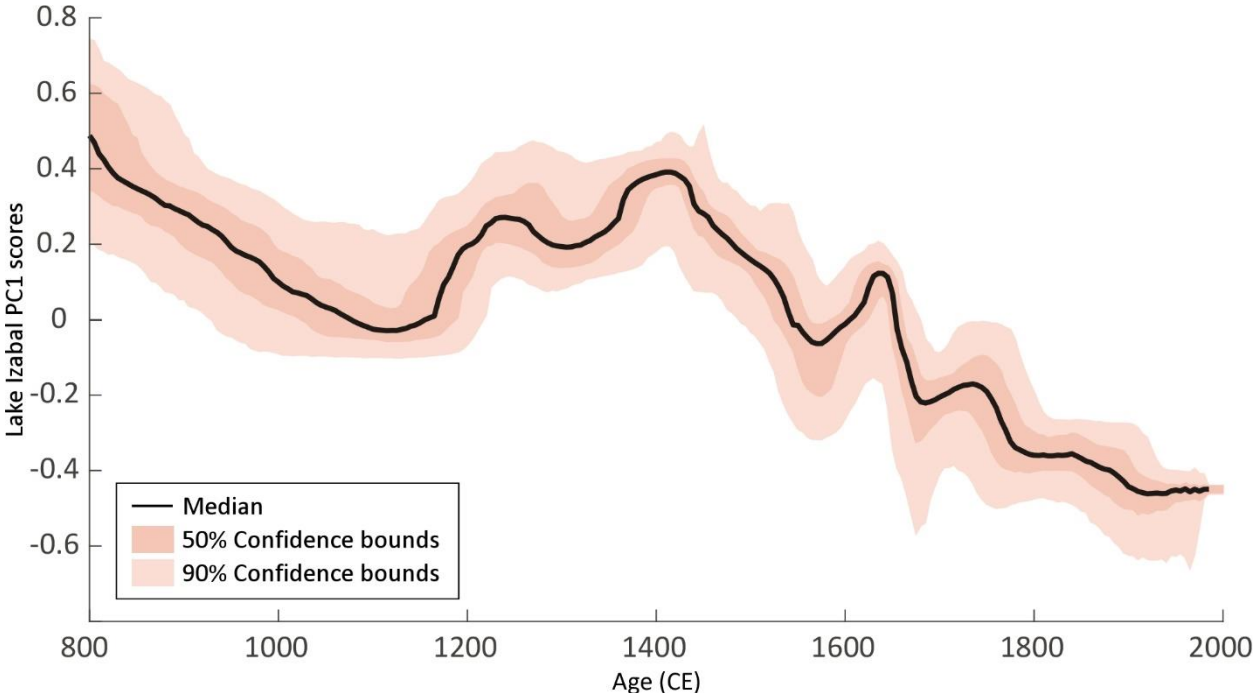

Figure S20. Median, 50% and 90% confidence bounds for the Lake Izabal PC1 scores (this study). The plot shows the range of proxy values for 1000 age-depth models (same set of models used for the correlation analysis shown in Figure 5). Note that the graph shows the unconditional probability at each time step. That is, the graph does not represent correlations between time steps.

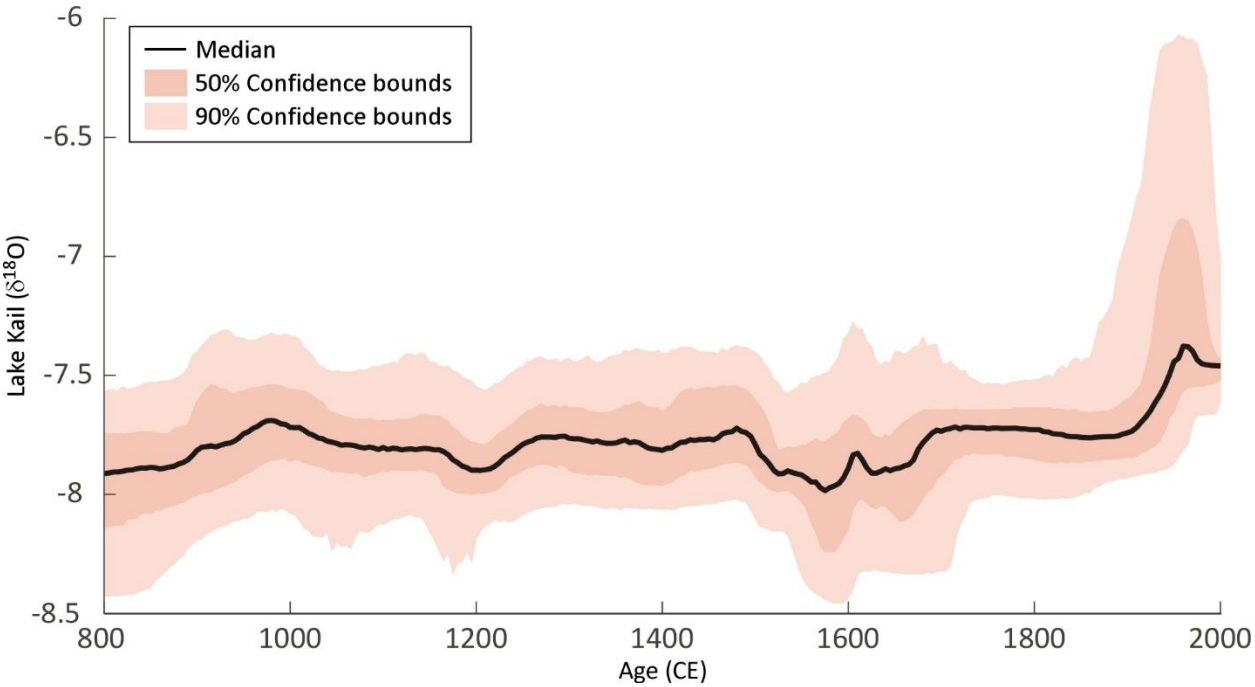

Figure S21. Median, 50% and 90% confidence bounds for the Lake Kail $\delta^{18}O$ record (Stansell et al., 2020). The plot shows the range of proxy values for 1000 age-depth models (same set of models used for the correlation analysis shown in Figure 5). Note that the graph shows the unconditional probability at each time step. That is, the graph does not represent correlations between time steps.

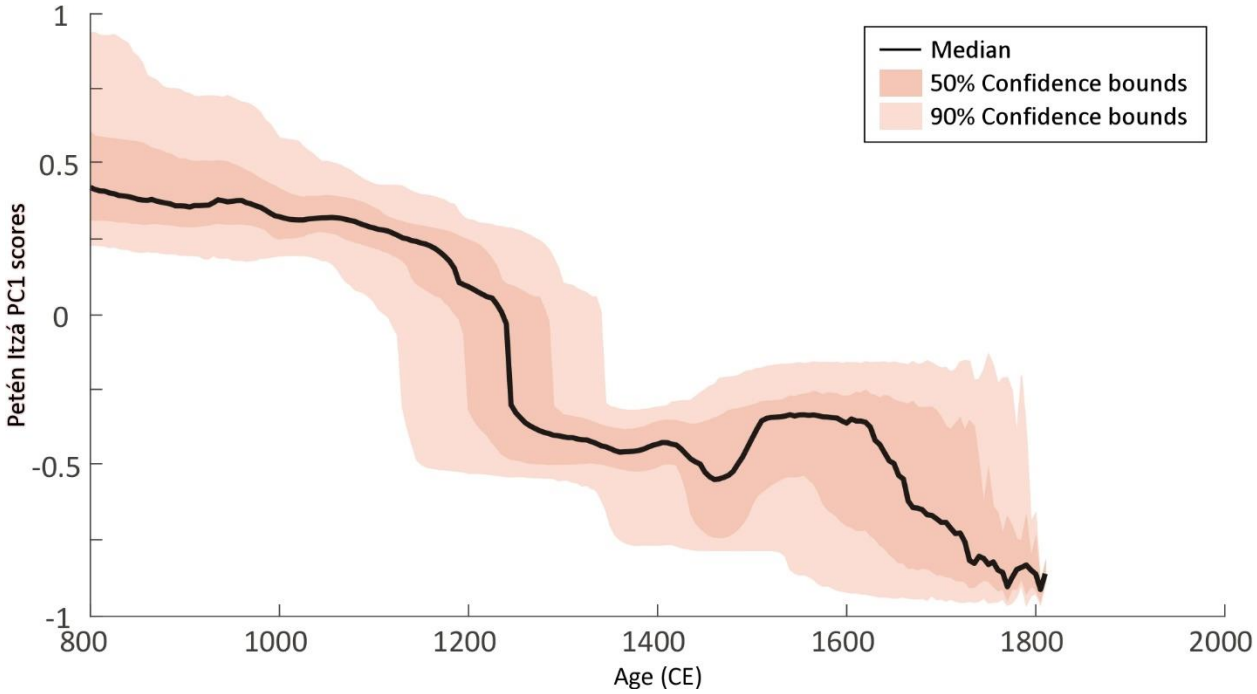

Figure S22. Median, 50% and 90% confidence bounds for the Lake Petén Itzá PC1 scores (this study). The plot shows the range of proxy values for 1000 age-depth models (same set of models used for the correlation analysis shown in Figure 5). Note that the graph shows the unconditional probability at each time step. That is, the graph does not represent correlations between time steps.

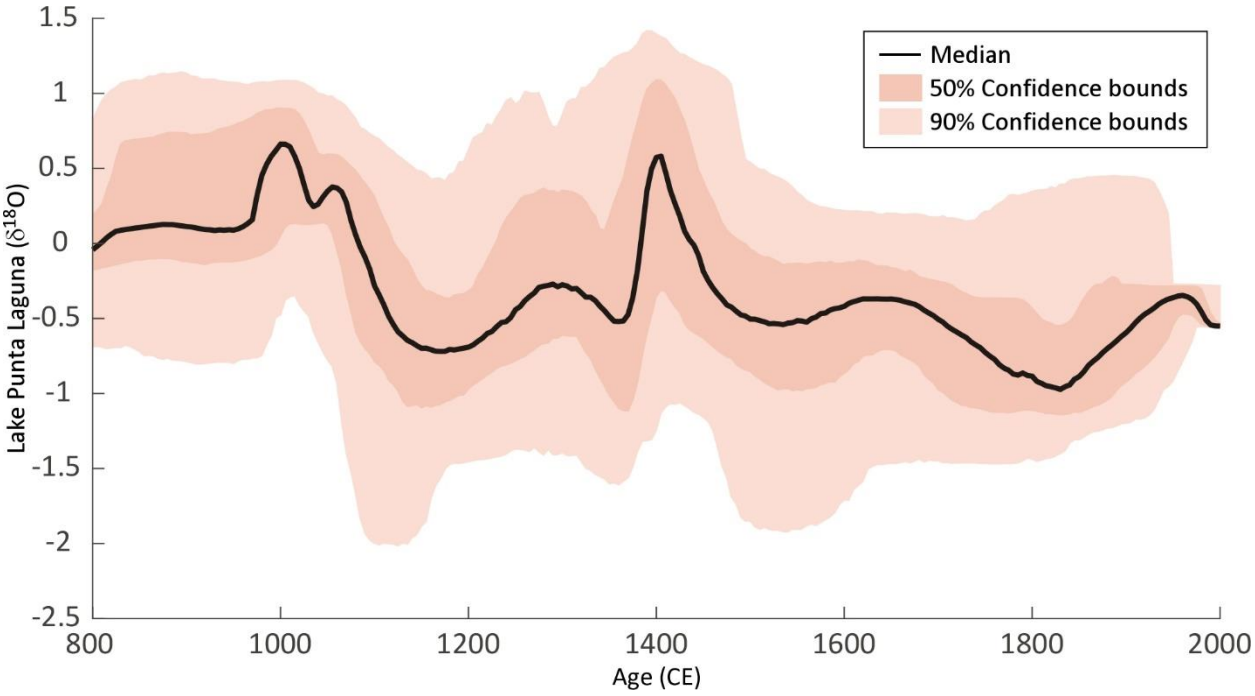

Figure S23. Median, 50% and 90% confidence bounds for the Punta Laguna $\delta^{18}O$ record (Curtis et al., 1996). The plot shows the range of proxy values for 1000 age-depth models (same set of models used for the correlation analysis shown in Figure 5). Note that the graph shows the unconditional probability at each time step. That is, the graph does not represent correlations between time steps.

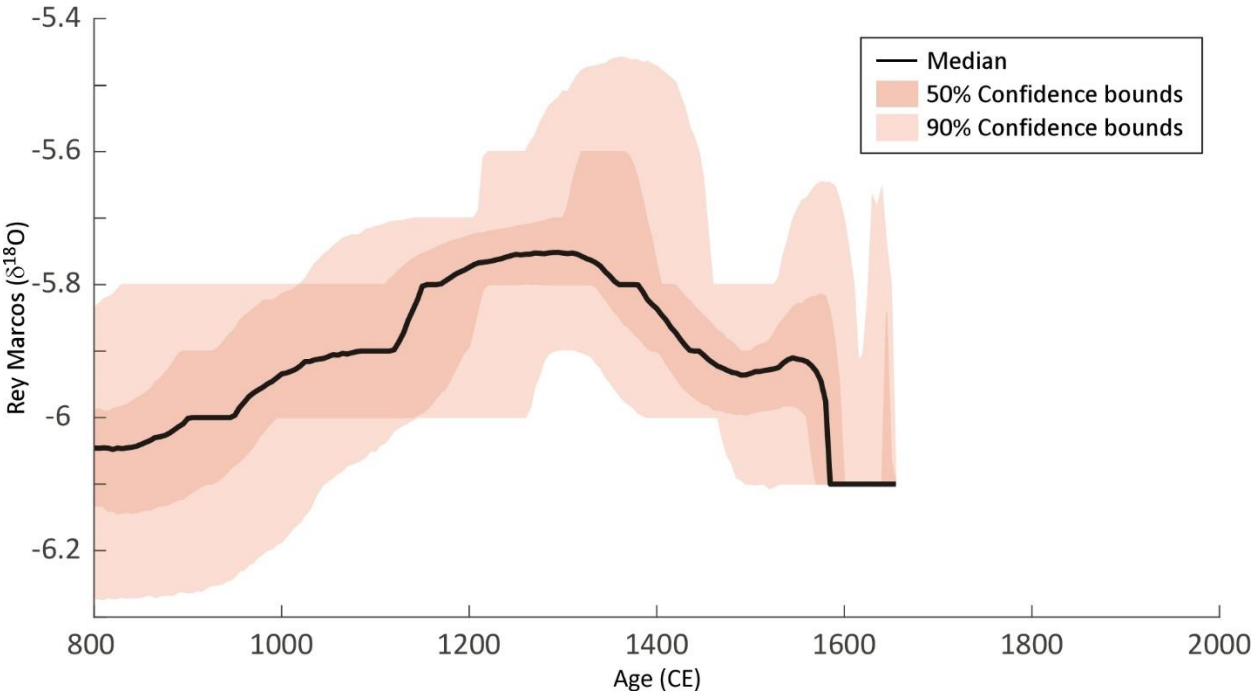

Figure S24. Median, 50% and 90% confidence bounds for the Rey Marcos speleothem $\delta^{18}O$ record (Winter et al., 2020). The plot shows the range of proxy values for 1000 age-depth models (same set of models used for the correlation analysis shown in Figure 5). Note that the graph shows the unconditional probability at each time step. That is, the graph does not represent correlations between time steps.

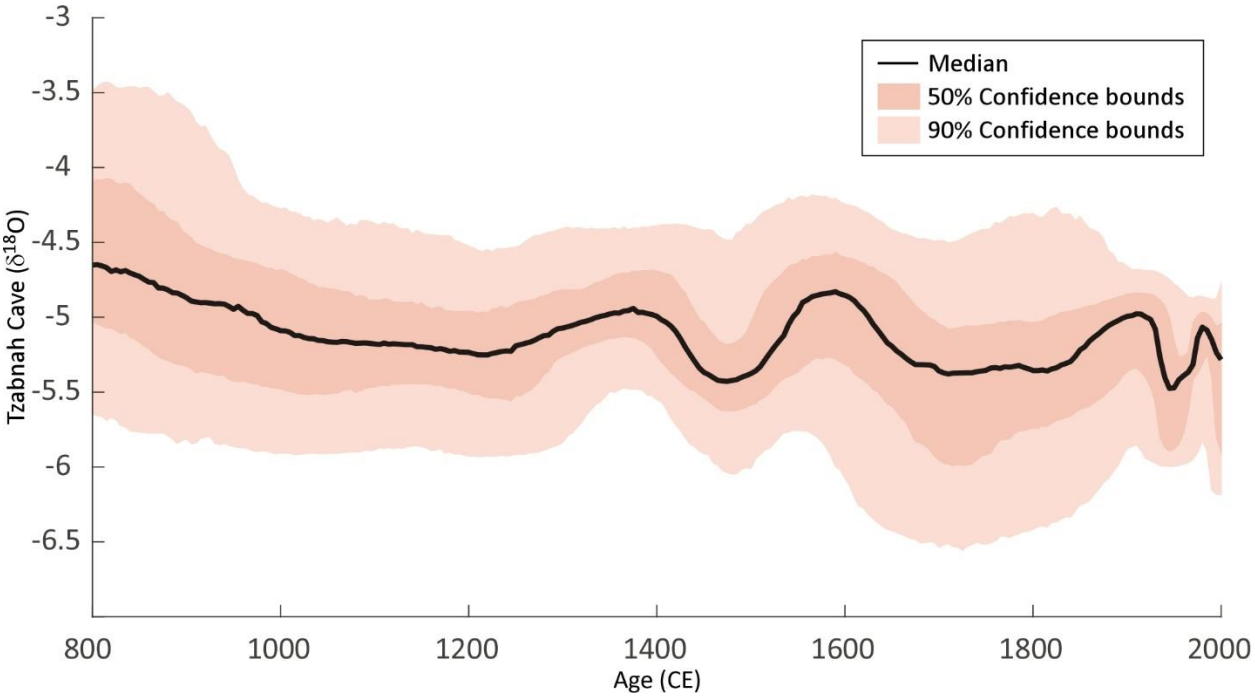

Figure S25. Median, 50% and 90% confidence bounds for the Tzabnah Cave speleothem $\delta^{18}O$ record (Medina-Elizalde et al., 2010). The plot shows the range of proxy values for 1000 age-depth models (same set of models used for the correlation analysis shown in Figure 5). Note that the graph shows the unconditional probability at each time step. That is, the graph does not represent correlations between time steps.

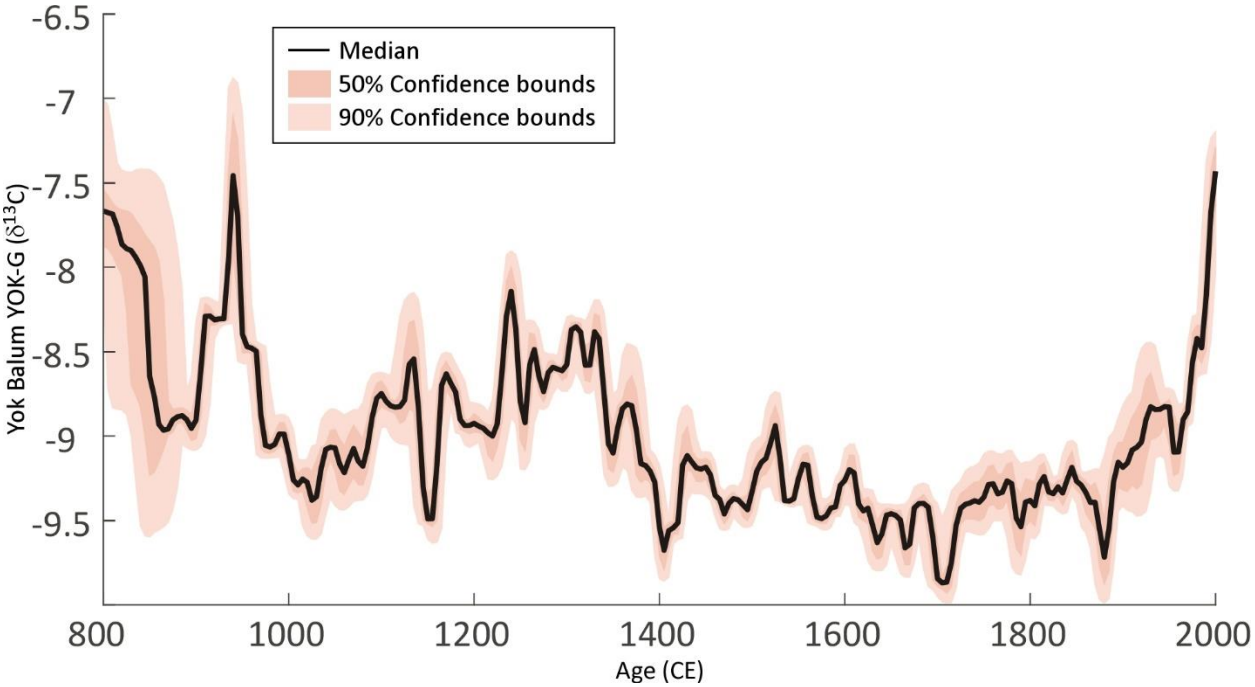

Figure S26. Median, 50% and 90% confidence bounds for the Yok Balum YOK-G speleothem $\delta^{13}C$ record (Asmerom et al., 2020). The plot shows the range of proxy values for 1000 age-depth models (same set of models used for the correlation analysis shown in Figure 5). Note that the graph shows the unconditional probability at each time step. That is, the graph does not represent correlations between time steps.

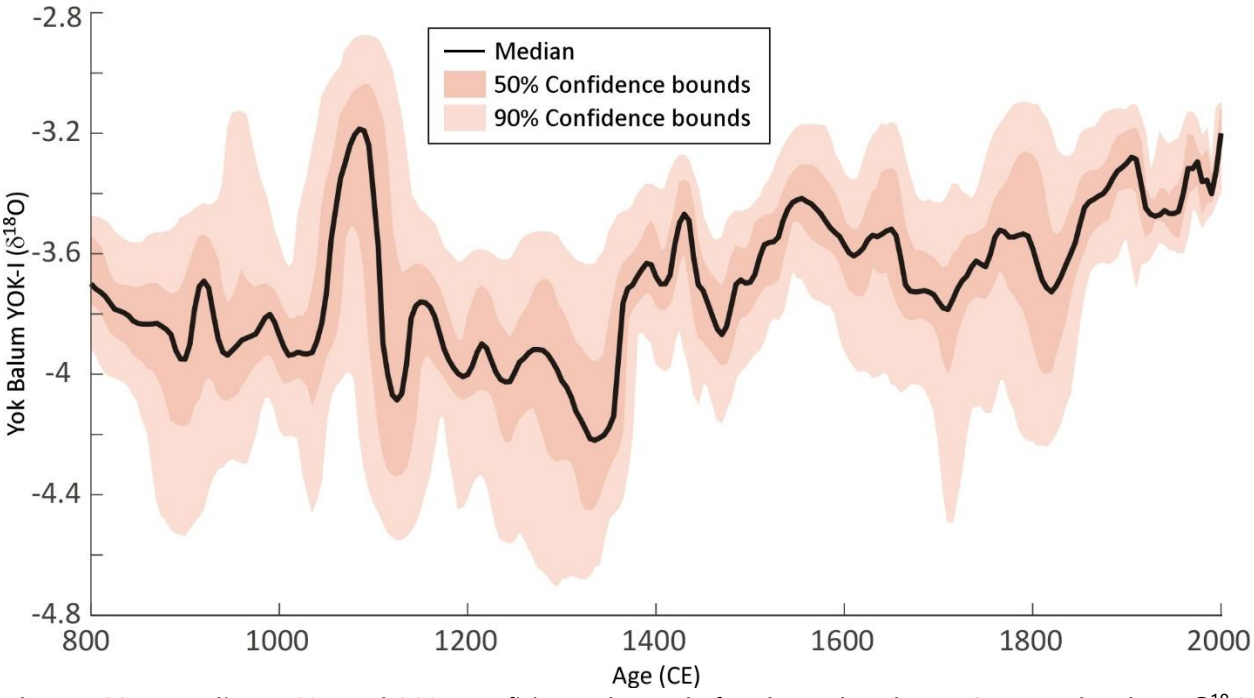

Figure S27. Median, 50% and 90% confidence bounds for the Yok Balum YOK-I speleothem $\delta^{18}O$ record (Kennett et al., 2012). The plot shows the range of proxy values for 1000 age-depth models (same set of models used for the correlation analysis shown in Figure 5). Note that the graph shows the unconditional probability at each time step. That is, the graph does not represent correlations between time steps.

References

Asmerom, Y., Baldini, J. U. L., Prufer, K. M., Polyak, V. J., Ridley, H. E., Aquino, V. V., et al. (2020). Intertropical convergence zone variability in the Neotropics during the Common Era. *Science Advances, 6*(7), eaax3644. https://doi.org/10.1126/sciadv.aax3644

Blaauw, M., & Christen, J. A. (2011). Flexible paleoclimate age-depth models using an autoregressive gamma process. *Bayesian Anal., 6*(3), 457-474. https://projecteuclid.org:443/euclid.ba/1339616472

Curtis, J. H., Hodell, D. A., & Brenner, M. (1996). Climate variability on the Yucatan Peninsula (Mexico) during he past 3500 years, and implications for Maya cultural evolution. *Quaternary Research, 46*(1), 37-47. https://doi.org/10.1006/qres.1996.0042

Harris, I., Jones, P. D., Osborn, T. J., & Lister, D. H. (2014). Updated high-resolution grids of monthly climatic observations – the CRU TS3.10 Dataset. *International Journal of Climatology, 34*(3), 623-642. https://doi.org/10.1002/joc.3711

Haug, G. H., Hughen, K. A., Sigman, D. M., Peterson, L. C., & Röhl, U. (2001). Southward migration of the Intertropical Convergence Zone through the Holocene. *Science, 293*(5533), 1304. https://doi.org/10.1126/science.1059725

Hernández, E., Obrist-Farner, J., Brenner, M., Kenney, W. F., Curtis, J. H., & Duarte, E. (2020). Natural and anthropogenic sources of lead, zinc, and nickel in sediments of Lake Izabal,

Guatemala. *Journal of Environmental Sciences, 96*, 117-126. https://doi.org/10.1016/j.jes.2020.04.020

Hodell, D. A., Brenner, M., Curtis, J. H., Medina-González, R., Ildefonso-Chan Can, E., Albornaz-Pat, A., & Guilderson, T. P. (2005). Climate change on the Yucatan Peninsula during the Little Ice Age. *Quaternary Research, 63*(2), 109-121. https://doi.org/10.1016/j.yqres.2004.11.004

Kennett, D. J., Breitenbach, S. F. M., Aquino, V. V., Asmerom, Y., Awe, J., Baldini, J. U. L., et al. (2012). Development and disintegration of Maya political systems in response to climate change. *Science, 338*(6108), 788-791. https://doi.org/10.1126/science.1226299

Medina-Elizalde, M., Burns, S. J., Lea, D. W., Asmerom, Y., von Gunten, L., Polyak, V., et al. (2010). High resolution stalagmite climate record from the Yucatán Peninsula spanning the Maya terminal classic period. *Earth and Planetary Science Letters, 298*(1), 255-262. https://doi.org/10.1016/j.epsl.2010.08.016

Obrist-Farner, J., & Rice, P. M. (2019). Nixtun-Ch'ich' and its environmental impact: Sedimentological and archaeological correlates in a core from Lake Petén Itzá in the southern Maya lowlands, Guatemala. *Journal of Archaeological Science: Reports, 26*, 101868. https://doi.org/10.1016/j.jasrep.2019.05.033

Reimer, P. J., Austin, W. E. N., Bard, E., Bayliss, A., Blackwell, P. G., Bronk Ramsey, C., et al. (2020). The IntCal20 Northern Hemisphere radiocarbon age calibration curve (0–55 cal kBP). *Radiocarbon, 62*(4), 725-757. https://doi.org/10.1017/RDC.2020.41

Schneider, U., Becker, A., Finger, P., Meyer-Christoffer, A., Rudolf, B., & Ziese, M. (2011). *GPCC full data reanalysis version 6.0 at 0.5◦: monthly land-surface precipita-tion from rain-gauges built on GTS-based and historic data*. Retrieved from: https://doi.org/10.5676/dwd_gpcc/fd_m_v6_050

Stansell, N. D., Steinman, B. A., Abbott, M. B., Rubinov, M., & Roman-Lacayo, M. (2013). Lacustrine stable isotope record of precipitation changes in Nicaragua during the Little Ice Age and Medieval Climate Anomaly. *Geology, 41*(2), 151-154. https://doi.org/10.1130/G33736.1

Stansell, N. D., Steinman, B. A., Lachniet, M. S., Feller, J., Harvey, W., Fernandez, A., et al. (2020). A lake sediment stable isotope record of late-middle to late Holocene hydroclimate variability in the western Guatemala highlands. *Earth and Planetary Science Letters, 542*, 116327. https://doi.org/10.1016/j.epsl.2020.116327

Willmott, C. J., & Matsuura, K. (2001). *Terrestrial Air Temperature and Precipitation: Monthly and Annual Time Series (1950–1999), Version 5.0.1. Center for Climatic Research*. Retrieved from: http://climate.geog.udel.edu/~climate/html_pages/README.ghcn_ts2.html

Winter, A., Zanchettin, D., Lachniet, M., Vieten, R., Pausata, F. S. R., Ljungqvist, F. C., et al. (2020). Initiation of a stable convective hydroclimatic regime in Central America circa 9000 years BP. *Nature Communications, 11*(1), 716. https://doi.org/10.1038/s41467-020-14490-y